



Resonant Damping of Kink Modes in Solar Coronal Slabs

Hui Yu¹ · Bo Li¹  · Shaoxia Chen¹ ·
Mingzhe Guo¹ 

© Springer

Abstract We examine resonantly damped kink modes in straight coronal slabs, paying special attention to the effects of the formulation for the transverse density distribution (“profile”). We work in the framework of pressure-less, gravity-free, resistive magnetohydrodynamics, and we adopt the dissipative-eigenmode perspective. The density profile is restricted to be one-dimensional, but nonetheless allowed to take a generic form characterized by a continuous transition layer connecting a uniform interior to a uniform exterior. A dispersion relation (DR) is derived in the thin-boundary limit, yielding analytical expressions for the eigenfrequencies that generalize known results in various aspects. We find that the analytical rather than the numerical solutions to the thin-boundary DR serve better the purpose for validating our self-consistent resistive solutions. More importantly, the eigenfrequencies are found to be sensitive to profile specifications, the ratio of the imaginary to the real part readily varying by a factor of two when one profile is used in place of another. Our eigenmode computations are also examined in the context of impulsively excited kink waves, suggesting the importance of resonant absorption for sufficiently oblique components when the spatial scale of the exciter is comparable to the slab half-width.

Keywords: Magnetohydrodynamics; Coronal Seismology; Waves, Magnetohydrodynamic; Magnetic fields, Corona

1. Introduction

There has been ample observational evidence that the highly structured solar corona is replete with low-frequency waves and oscillations (see, *e.g.* De Moortel and Nakariakov, 2012; Nakariakov et al., 2016; Nakariakov and Kolotkov,

✉ B. Li
bbl@sdu.edu.cn

¹ Shandong Provincial Key Laboratory of Optical Astronomy and Solar-Terrestrial Environment, Institute of Space Sciences, Shandong University, Weihai, 264209 Shandong, China

2020; Li et al., 2020; Van Doorselaere et al., 2020a; Wang et al., 2021, for recent reviews). A customary practice, known as “coronal seismology” or more broadly “solar atmospheric seismology”, is then to place these observations in the theoretical framework of magnetohydrodynamic (MHD) waves in structured media, allowing one to infer the atmospheric parameters that prove difficult to directly measure (for recent topical collections, see, *e.g.* Ballester et al., 2007; Nakariakov and Erdélyi, 2009; Erdélyi and Goossens, 2011; Van Doorselaere et al., 2020b). From the theoretical perspective, wave-hosting structures have long been modeled as density-enhanced cylinders embedded in an otherwise uniform corona (*e.g.* Rosenberg, 1970; Zajtsev and Stepanov, 1975; Spruit, 1982; Edwin and Roberts, 1983; Cally, 1986; see also the recent textbook by Roberts, 2019). The subsequent applications to kink modes in active-region (AR) loops, abundantly measured since the Transition Region and Coronal Explorer era (TRACE, Aschwanden et al., 1999; Nakariakov et al., 1999), then enabled the inference of the magnetic-field strength not only for individual loops (Nakariakov and Ofman, 2001) but also over a substantial portion of an AR (Anfinogentov and Nakariakov, 2019) or even across several ARs (Yang et al., 2020). While the axial phase speeds alone suffice for this purpose, the damping rates of coronal kink modes have also proved informative for inferring the information on the transverse density distribution (*e.g.* Aschwanden et al., 2003; Arregui et al., 2007b; Goossens et al., 2008; Arregui and Asensio Ramos, 2014), provided that the damping can be accounted for by the resonant absorption in the Alfvén continuum (*e.g.* Ruderman and Roberts, 2002; Goossens, Andries, and Aschwanden, 2002). This information is known to be critical in wave-based mechanisms for coronal heating (*e.g.* Arregui, 2015; Cranmer and Winebarger, 2019) but difficult to glean (see, *e.g.* the remarks by Arregui and Goossens, 2019).

There is a long history of theoretical examinations on MHD waves in magnetized slabs as well, in both non-solar (*e.g.* Tataronis and Grossmann, 1973; Grossmann and Tataronis, 1973; Hasegawa and Chen, 1974; Chen and Hasegawa, 1974) and solar contexts (*e.g.* Ionson, 1978; Wentzel, 1979a; Edwin and Roberts, 1982). Focusing on the solar context, these examinations are not only important in their own right but prove necessary given the diversity of solar atmospheric structures (for recent studies, see, *e.g.* Hornsey, Nakariakov, and Fludra, 2014; Allcock and Erdélyi, 2017; Oxley, Zsámberger, and Erdélyi, 2020). Further restricting ourselves to coronal kink modes, we note that a slab configuration is indeed more relevant for interpreting such observations as sunward moving tadpoles in post-flare supra-arcades (Verwichte, Nakariakov, and Cooper, 2005), oscillating AR arcades in response to flaring activities (Jain, Maurya, and Hindman, 2015; Allian, Jain, and Hindman, 2019), and large-scale propagating transverse motions of streamer stalks (“streamer waves”, Chen et al., 2010, 2011; Decraemer, Zhukov, and Van Doorselaere, 2020). The application of a slab equilibrium to streamer waves seems somehow surprising given the current sheets embedded in streamer stalks, but it is actually justifiable provided that current sheets can be regarded as infinitely thin and the electric resistivity can be neglected (*e.g.* Edwin, Roberts, and Hughes, 1986; Feng et al., 2011).

This study is intended to examine resonantly damped kink modes in pressureless, straight coronal slabs structured in a one-dimensional (1D) manner, and it

can be regarded as an extension of the study by Arregui et al. (2007a, A07 hereafter). For the ease of discussion, let the slab axis be directed in the z -direction. By “1D” we refer to a configuration where the equilibrium density is nonuniform only in the x -direction, but it nonetheless takes a rather generic form comprising a transition layer (TL) that continuously connects a uniform interior to a uniform tenuous exterior. We further denote the axial and out-of-plane wavenumbers by k_z and k_y , respectively. For the configuration at hand, an extensive list of analytical studies has established that obliquely propagating ($k_y \neq 0$) kink modes are resonantly absorbed in the Alfvén continuum, provided that the TL width is finite ($l \neq 0$) (*e.g.* Ionson, 1978; Wentzel, 1979a; Hollweg and Yang, 1988). To our knowledge, these studies tend to assume that $k_y \gg k_z$ and $k_y l \ll 1$, which were first lifted in the numerical study of A07. However, among the many observationally relevant parameters, only the influence of k_y was examined therein for a particular density profile specification (“profile” for brevity). Our study therefore differs from A07 in the following three ways: First, we will numerically explore a broader set of parameters for the same specification and additionally examine two different profiles. The former aspect is necessary to address, given the evident influence of such additional parameters as the TL width on the damping rate. On the other hand, although exclusively pertaining to the case where $k_y = 0$, previous results have demonstrated the profile sensitivity of the dispersive properties of kink modes (*e.g.* Edwin and Roberts, 1988; Lopin and Nagorny, 2015; Yu et al., 2015; Chen et al., 2018b). Drawing analogy with pertinent cylindrical studies (Soler et al., 2013, 2014), one expects the same sensitivity for a non-vanishing k_y given that cylindrical results tend to be closely connected to slab ones when k_y is substantial (*e.g.* Goossens, Hollweg, and Sakurai, 1992). Second, we will also provide analytical expressions for the eigenfrequencies in some limiting situations. While our approach is much-practiced, we will show that these expressions extend known solar results by allowing a broader range of k_y and non-solar results by allowing rather general profile choices. Third, we will connect our computations to impulsively generated kink waves, as likely to be relevant for, say, streamer waves. On this aspect we note that resonant absorption has been invoked to account for the rapid damping of the oscillatory motions of streamer stalks imaged with the COR1 coronagraph on board the Solar TERrestrial RELations Observatory (STEREO/COR1, Kwon et al., 2013, Figure 6). We note that the pertinent cylindrical theories were implicated therein, despite that a slab configuration seems more appropriate (*e.g.* Decraemer, Zhukov, and Van Doorselaere, 2019).

This article is organized as follows. Section 2 details the specification of our equilibrium configuration, and how we formulate and solve the pertinent eigenvalue problem. The numerical results are then presented in Section 3. Section 4 summarizes the present study, ending with some concluding remarks.

2. Model Description

2.1. Equilibrium Configuration

We adopt resistive, gravity-free MHD throughout, and additionally we neglect the gas pressure. The primitive variables are then the mass density $[\rho]$, velocity $[\mathbf{v}]$, and magnetic field $[\mathbf{B}]$. We denote the equilibrium quantities with the subscript 0, and assume that no equilibrium flow is present ($\mathbf{v}_0 = 0$). Working in a Cartesian coordinate system (x, y, z) , we take the equilibrium magnetic field to be uniform and directed in the z -direction ($\mathbf{B}_0 = B_0 \hat{\mathbf{z}}$). We take the equilibrium density $[\rho_0]$ to be structured only in the x -direction and symmetric about $x = 0$. The transverse profile for ρ_0 is further assumed to comprise a uniform interior with density ρ_i , a uniform exterior with density ρ_e , and a transition layer (TL) continuously connecting the two ($\rho_i > \rho_e$). The Alfvén speed is defined by $v_A^2 = B_0^2/(\mu_0 \rho_0)$, where μ_0 is the magnetic permeability in free space. We denote the values of v_A in the interior and exterior by v_{Ai} and v_{Ae} , respectively. To specify the density profile, it suffices to consider only the half-space $x \geq 0$,

$$\rho_0(x) = \begin{cases} \rho_i, & 0 \leq x < x_i = R - l/2, \\ \rho_{tr}(x), & x_i \leq x \leq x_e = R + l/2, \\ \rho_e, & x > x_e. \end{cases} \quad (1)$$

It is evident that this configuration mimics a density-enhanced slab of mean half-width R embedded in a uniform ambient. In addition, the TL width $[l]$ lies in the range between 0 and $2R$. A number of much-employed TL profiles will be examined, namely (*e.g.* Ruderman and Roberts, 2002; Soler et al., 2013; Yu et al., 2015)

$$\rho_{tr}(x) = \begin{cases} \frac{\rho_i}{2} \left[\left(1 + \frac{\rho_e}{\rho_i} \right) - \left(1 - \frac{\rho_e}{\rho_i} \right) \sin \frac{\pi(x-R)}{l} \right], & \text{sine,} \\ \rho_i - (\rho_i - \rho_e) \left(\frac{x-x_i}{l} \right), & \text{linear,} \\ \rho_i - (\rho_i - \rho_e) \left(\frac{x-x_i}{l} \right)^2, & \text{parabolic.} \end{cases} \quad (2)$$

We note that A07 was dedicated to a “sine” profile. Figure 1 illustrates both our equilibrium configuration and the density profiles. For illustrative purposes, the density contrast $[\rho_i/\rho_e]$ and the dimensionless TL width $[l/R]$ are chosen to be 10 and 0.75, respectively.

2.2. Formulation of the Eigenvalue Problem and Method of Solution

Let the subscript 1 denote small-amplitude perturbations to the equilibrium. The linearized resistive MHD equations then read

$$\rho_0 \frac{\partial \mathbf{v}_1}{\partial t} = \frac{(\nabla \times \mathbf{B}_1) \times \mathbf{B}_0}{\mu_0}, \quad (3)$$

$$\frac{\partial \mathbf{B}_1}{\partial t} = \nabla \times \left(\mathbf{v}_1 \times \mathbf{B}_0 - \frac{\eta}{\mu_0} \nabla \times \mathbf{B}_1 \right). \quad (4)$$

Here η is the Ohmic resistivity, taken to be constant for simplicity. We adopt an eigenvalue-problem (EVP) standpoint by Fourier-analyzing any perturbation as

$$f_1(x, y, z; t) = \text{Re}\{\tilde{f}(x) \exp[-i(\omega t - k_y y - k_z z)]\}, \quad (5)$$

where ω is the angular frequency, and k_z (k_y) represents the axial (out-of-plane) wavenumber. With tilde we denote the Fourier amplitude. We take k_y and k_z as real-valued, but allow ω to be complex-valued. If some quantity is complex, then we denote its real and imaginary parts with subscripts R and I, respectively. Note that $\omega_I < 0$ throughout. In component form, Equations 3 and 4 become

$$\omega \tilde{v}_x = -\frac{B_0}{\mu_0 \rho_0} \left(k_z \tilde{B}_x + i \tilde{B}'_z \right), \quad (6)$$

$$\omega \tilde{v}_y = -\frac{B_0}{\mu_0 \rho_0} \left(k_z \tilde{B}_y - k_y \tilde{B}_z \right), \quad (7)$$

$$\omega \tilde{B}_x = -B_0 k_z \tilde{v}_x + \frac{i\eta}{\mu_0} \left[\tilde{B}''_x - (k_y^2 + k_z^2) \tilde{B}_x \right], \quad (8)$$

$$\omega \tilde{B}_y = -B_0 k_z \tilde{v}_y + \frac{i\eta}{\mu_0} \left[\tilde{B}''_y - (k_y^2 + k_z^2) \tilde{B}_y \right], \quad (9)$$

$$\omega \tilde{B}_z = -iB_0 (\tilde{v}'_x + i k_y \tilde{v}_y) + \frac{i\eta}{\mu_0} \left[\tilde{B}''_z - (k_y^2 + k_z^2) \tilde{B}_z \right], \quad (10)$$

where we have used the shorthand notation $' \equiv d/dx$. Equations 6 to 10 constitute a standard EVP when supplemented with appropriate boundary conditions (BCs). With kink modes in mind, we specify the BCs at the slab axis ($x = 0$) as $\tilde{v}'_x = \tilde{v}_y = \tilde{B}'_x = \tilde{B}_y = \tilde{B}_z = 0$. Only trapped modes are of interest, in accordance with which all variables are required to vanish when $x \rightarrow \infty$.

The solution procedure for the EVP is as follows. We start with normalizing Equations 6 to 10, for which purpose we take R , v_{Ai} , and ρ_i as the independent normalizing constants. The derivative normalizing constants for time and magnetic field are chosen to be R/v_{Ai} and $B_i \equiv \sqrt{\mu_0 \rho_i v_{Ai}^2}$, respectively. The Ohmic resistivity is wrapped up in the magnetic Reynolds number $R_m = \mu_0 R v_{Ai} / \eta$. We formulate and solve the EVP with the general-purpose finite-element code PDE2D (Sewell, 1988), which was first introduced into the solar context by Terradas, Oliver, and Ballester (2006) to our knowledge. We adopt a computational domain of $[0, x_M]$, and place the outer boundary $[x_M]$ sufficiently far from the slab such that further increasing x_M does not influence our numerical results.

A nonuniform grid is employed to save computational cost, and a considerable fraction of the grid points is deployed in the TL to resolve the possible oscillatory behavior therein. It turns out that the details of the grid setup have some bearings on the parameter range that we can explore. To illustrate this, we recall that the resistive approach here is not intended to explore the full spectrum of resistive eigenmodes. Rather, we are interested only in the one that falls back to the standard kink mode when the TL is infinitely thin ($l = 0$) and the resistivity vanishes ($\eta = 0$). Allowing l to be finite, we are adopting the well known resistive eigenmode approach to examine the essentially ideal process of the resonant absorption of a collective mode in the relevant continuum (*e.g.* Poedts and Kerner, 1991; Van Doorselaere et al., 2004; Terradas, Oliver, and Ballester, 2006; Guo et al., 2016; Chen et al., 2018a) or continua (*e.g.* Soler et al., 2009; Chen et al., 2021). As such, we are looking for only those eigenfrequencies that do not depend on R_m when R_m is sufficiently large. This is illustrated by Figure 2 where the ratio of the imaginary to the real part of the eigenfrequency (or $-\omega_I/\omega_R$ to be precise) is shown as a function of the magnetic Reynolds number $[R_m]$ for a “sine” density profile with $\rho_i/\rho_e = 10$. In addition, $[k_y R, k_z R]$ is fixed at $[1, \pi/50]$. A series of l/R , equally spaced by 0.01, is examined except for the lowermost curve. The outer boundary is fixed at $x_M = 50 R$. Furthermore, 18000 uniformly spaced grid points are employed for $x \leq 3 R$, beyond which the grid spacing increases by a constant factor of 1.00125. For a given l/R , one sees that the eigenfrequencies are indeed R_m -independent over an interval of R_m , for which the left and right ends are to be denoted by $R_{m,L}$ and $R_{m,R}$, respectively. Evidently, the sought-after eigenfrequencies can be confidently identified only when the interval $[R_{m,L}, R_{m,R}]$ is sufficiently broad. However, this cannot be guaranteed. On the one hand, $R_{m,L}$ tends to increase with l/R . On the other hand, our code does not converge when R_m becomes too large for the well known reason that the eigenfunctions become increasingly oscillatory in the so-named dissipative layers (DLs) (see, *e.g.* Figure 4 in Ruderman, Tirry, and Goossens, 1995; Figure 1 in Tirry and Goossens, 1996). On top of that, Figure 2 indicates that some zigzags appear when R_m approaches the maximal value that the code can handle, the end result being that the interval $[R_{m,L}, R_{m,R}]$ narrows with l/R . Overall, we find that this numerical difficulty arises when the damping is heavy, which occurs when l/R and/or $k_y R$ are large. Numerically speaking, this interval can be made broader by employing more grid points to resolve the fine scales in the DLs. In practice, we experiment with a substantial number of grid setups such that we can expand the parameter range examined by A07 where the “sine” profile is adopted. In addition, we will examine another two profiles stated in Equation 2. The purpose of presenting Figure 2 is to illustrate the R_m -dependence of the eigen-frequencies of resonantly damped kink modes in coronal slabs, thereby complementing cylindrical studies with similar scopes (*e.g.*, Figure 2 in Terradas, Oliver, and Ballester, 2006; Figure 9 in Guo et al., 2016).

For ease of description, we formally express the eigenfrequencies as

$$\frac{\omega R}{v_{Ai}} = \mathcal{G} \left(\text{prof}, \frac{\rho_i}{\rho_e}, \frac{l}{R}; k_y R, k_z R \right), \quad (11)$$

where “prof” represents a prescription for the equilibrium density profile. The magnetic Reynolds number does not appear in Equation 11, which means in practice that the computed eigenfrequencies are found in an interval of $[R_{m,L}, R_{m,R}]$ spanning at least half a decade or so.

2.3. Resonantly Damped Kink Modes in the Thin-Boundary Limit

The functional dependence in Equation 11 can be established analytically in a number of situations. This subsection is intended to expand some available results, for which purpose we start by noting that the ideal version ($\eta = 0$) of Equations 6 to 10 can be manipulated to yield a single equation governing \tilde{v}_x (*e.g.* A07), namely

$$\left[\frac{k_z^2 - \omega^2/v_A^2}{k_y^2 + k_z^2 - \omega^2/v_A^2} \tilde{v}_x' \right]' - (k_z^2 - \omega^2/v_A^2) \tilde{v}_x = 0. \quad (12)$$

Evidently, the Alfvén resonance takes place at $x = x_A$ where $\omega_R = k_z v_A$. We now distinguish between two schools of approaches for treating resonantly damped modes. In one school, broadly referred to as the ideal quasi-mode approach, dissipative effects are mathematically irrelevant and a non-vanishing ω_I is accounted for by, say, analytically continuing the Green function (for early studies in various contexts, see, *e.g.* Tataronis and Grossmann, 1973; Grossmann and Tataronis, 1973; Hasegawa and Chen, 1974; Chen and Hasegawa, 1974; Ionson, 1978; Wentzel, 1979b; see also the review by Goossens, Erdélyi, and Ruderman, 2011). Equation 12 is involved in a substantial number of quasi-mode studies, which tend to assume $k_y^2 \gg k_z^2$ and $k_y^2 \gg |k_z^2 - \omega^2/v_A^2|$ from the outset, and address a “linear” profile. Of particular relevance is the one in the fusion context by Tatsuno and Wakatani (1998, hereafter TW98; see also references therein), who showed that adopting a linear profile enables one to derive an analytical dispersion relation (DR) valid for arbitrary TL widths. As a result, the resonant damping is allowed to be heavy. Another school, referred to as the dissipative eigenmode approach and hence involving dissipative factors by construction, does not restrict the range of k_y but nonetheless assumes weak damping by working in the so-called thin-boundary (TB) limit ($l/R \ll 1$). However, no restriction is necessary for the equilibrium profile (*e.g.* Sakurai, Goossens, and Hollweg, 1991; Goossens, Hollweg, and Sakurai, 1992; Ruderman, Tirry, and Goossens, 1995, to name only a few). We will follow the second approach.

We proceed by defining

$$\kappa_{i,e}^2 = k_z^2 - \frac{\omega^2}{v_{Ai,e}^2}, \quad (13)$$

$$m_{i,e}^2 = k_y^2 + k_z^2 - \frac{\omega^2}{v_{Ai,e}^2}, \quad (14)$$

where $-\pi/2 < \arg \kappa_{i,e}, \arg m_{i,e} \leq \pi/2$. Trapped kink modes then correspond to the following solution to Equation 12 in the uniform portions

$$\tilde{v}_x(x) = \begin{cases} A_1 \cosh(m_i x), & 0 < x < x_i, \\ A_2 \exp(-m_e x), & x > x_e, \end{cases} \quad (15)$$

where A_1 and A_2 are constants. In addition, the Fourier amplitude of the Eulerian perturbation of total pressure ($p_{\text{tot}} = \mathbf{B}_0 \cdot \mathbf{B}_1 / \mu_0 = B_0 B_{1z} / \mu_0$) reads

$$\tilde{p}_{\text{tot}}(x) = \begin{cases} \left(\frac{B_0^2}{\mu_0} \right) \left(\frac{-iA_1}{\omega} \right) \left(\frac{\kappa_i^2}{m_i} \right) \sinh(m_i x), & 0 < x < x_i, \\ \left(\frac{B_0^2}{\mu_0} \right) \left(\frac{iA_2}{\omega} \right) \left(\frac{\kappa_e^2}{m_e} \right) \exp(-m_e x), & x > x_e. \end{cases} \quad (16)$$

Let $\{q\}$ denote the variation of some perturbation q across some thin dissipative layer bracketing the resonance. Furthermore, let $\tilde{\xi}_x$ denote the Fourier amplitude of the x -component of the Lagrangian displacement ($\tilde{v}_x = -i\omega\tilde{\xi}_x$). Assuming $l/R \ll 1$, the TB approximation attributes the variation of q across the TL to $\{q\}$, and $\{\tilde{p}_{\text{tot}}\}$ and $\{\tilde{\xi}_x\}$ were found to be (*e.g.* Tirry and Goossens, 1996; Andries, Tirry, and Goossens, 2000)

$$\{\tilde{p}_{\text{tot}}\} = 0, \quad (17)$$

$$\{\tilde{\xi}_x\} = -\frac{i\pi k_y^2 \text{sgn}(\omega_R)}{\rho_A |\Delta_A|} \tilde{p}_{\text{tot},A}, \quad (18)$$

where any quantity designated with a subscript A is evaluated at the Alfvén resonance. Equations 17 and 18 are a slab generalization of the cylindrical version established by Sakurai, Goossens, and Hollweg (1991). The symbol Δ_A was also introduced therein, and reads for the present slab configuration

$$\Delta_A = \frac{d(\omega^2 - k_z^2 v_A^2)}{dx} \Big|_{x=x_A}. \quad (19)$$

With the jump conditions (Equations 17 and 18), one can connect \tilde{v}_x and \tilde{p}_{tot} in the interior and exterior, thereby establishing the following DR

$$\coth(m_i R) = -\left(\frac{\kappa_i^2}{\kappa_e^2} \right) \left(\frac{m_e}{m_i} \right) + i\pi \left(\frac{k_y^2}{k_z^2} \right) \left(\frac{\rho_A}{\rho'_A} \right) \left(\frac{\kappa_i^2}{m_i} \right). \quad (20)$$

Here ω_R is taken to be positive without loss of generality. We have also used the fact that $v_A^2(x) \propto 1/\rho(x)$ and $\rho' < 0$ in our equilibrium setup.

Equation 20 is analytically tractable when one assumes that $k_y^2 \gg |\omega^2/v_A^2|$, in which case $m_i \approx m_e \approx k_y$. Further assuming that $k_y l \ll 1$ and $|\omega_I| \ll \omega_R$, one proceeds by keeping only the terms linear in ω_I . The real part of the right-hand side (RHS) of Equation 20 is dominated by the first term, resulting in

$$\omega_R^2 = k_z^2 v_{Ai}^2 \frac{1 + \Theta}{\rho_e/\rho_i + \Theta}, \quad (21)$$

where $\Theta = \tanh(k_y R)$. With the aid of Equation 21, the leading terms of the imaginary part of Equation 20 lead to that

$$\frac{\omega_I}{\omega_R} = -\frac{\pi}{2} \left(k_y \left| \frac{\rho_A}{\rho'_A} \right| \right) \frac{(1 - \rho_e/\rho_i)^2 \Theta^2}{(\rho_e/\rho_i + \Theta)^2 (1 + \Theta)}. \quad (22)$$

As intuitively expected, ω_R as given by Equation 21 does not involve the specific prescription for the density profile. Consequently, the density at the resonance always evaluates to $\rho_A = (\rho_e + \Theta \rho_i)/(1 + \Theta)$. However, the profile specification does influence ω_I through the ρ'_A -term in Equation 22. To evaluate this term, it can be readily found that the resonance takes place at

$$\frac{x_A - R}{l} = \begin{cases} \frac{1}{\pi} \arcsin \left(\frac{1 - \Theta}{1 + \Theta} \right), & \text{sine,} \\ \frac{1}{1 + \Theta} - \frac{1}{2}, & \text{linear,} \\ \left(\frac{1}{1 + \Theta} \right)^{1/2} - \frac{1}{2}, & \text{parabolic.} \end{cases} \quad (23)$$

It then follows that

$$\rho'_A = - \left(\frac{\rho_i - \rho_e}{l} \right) \frac{1}{g}, \quad (24)$$

where

$$g = \begin{cases} \frac{1 + \Theta}{\pi \sqrt{\Theta}}, & \text{sine,} \\ 1, & \text{linear,} \\ \left(\frac{1 + \Theta}{4} \right)^{1/2}, & \text{parabolic.} \end{cases} \quad (25)$$

Eventually, the TB damping rate can be expressed as

$$\frac{\omega_I}{\omega_R} = -\frac{\pi}{2} (k_y l) g \frac{(1 - \rho_e/\rho_i) \Theta^2}{(\rho_e/\rho_i + \Theta)(1 + \Theta)^2}. \quad (26)$$

Some remarks are necessary to address the assumption $k_y l \ll 1$. When deriving Equation 21, we neglected the second term on the RHS of Equation 20. Now with Equation 22 available, we can go back to Equation 20 and evaluate the real part of the second term on its RHS. To maintain consistency, this real part should be far smaller than the LHS, which evaluates to $1/\Theta$. The end result is that the following inequality should be valid,

$$\left[\pi k_y \left(\frac{\rho_A}{\rho'_A} \right) \right]^2 \frac{(1 - \rho_e/\rho_i)^2 \Theta^3}{(\rho_e/\rho_i + \Theta)^3} \ll 1.$$

Specializing to the profiles in this study, we find with Equation 24 that

$$(k_y l)^2 (\pi g)^2 \frac{\Theta^3}{(1 + \Theta)^2 (\rho_e/\rho_i + \Theta)} \ll 1.$$

By requiring $k_y l \ll 1$ we actually mean the situations where the afore-mentioned inequalities hold, which may be less restrictive.

We now compare our TB expressions with some previous results. We start by considering a further limit where $k_y R$ is large enough to ensure $\Theta \approx 1$. In this case, Equation 21 simplifies to

$$\omega_R^2 = \omega_k^2 \equiv k_z^2 c_k^2, \quad (27)$$

where

$$c_k^2 = \frac{2v_{Ai}^2}{1 + \rho_e/\rho_i} \quad (28)$$

defines the kink speed. Likewise, Equation 26 yields that

$$\frac{\omega_I}{\omega_R} = -\frac{\pi}{8} (k_y l) g \frac{\rho_i - \rho_e}{\rho_i + \rho_e}. \quad (29)$$

To proceed, we note that g now evaluates to $2/\pi$, 1, and $1/\sqrt{2}$ for the sine, linear, and parabolic profiles, respectively. Consider the linear profile for now. Equation 29 recovers the cylindrical result obtained by Goossens, Hollweg, and Sakurai (1992, Equation 79b), who were the first to adopt the jump conditions to examine quasi-modes from the dissipative-eigenmode perspective to our knowledge. As suggested therein, the comparison between the slab and cylindrical configurations is possible by interpreting R as the cylinder radius and prescribing k_y with $1/R$. Indeed, adopting this prescription in Equation 29 further recovers the cylindrical results for the sine (Ruderman and Roberts, 2002, Equation 72) and parabolic profiles (Soler et al., 2014, Equation 7). Now we focus on the slab configuration. For a linear profile, Equations 27 and 29 have been obtained in an extensive series of studies using the ideal quasi-mode approach (*e.g.* Ionson, 1978; Wentzel, 1979a, to name only a few early studies). Among the quasi-mode studies, to our knowledge, TW98 were the only one that offered explicit expressions for the eigenfrequencies without requiring $\Theta \approx 1$. It is reassuring to see that Equation 15 therein is exactly reproduced by our Equations 21 and 26, which are derived with the dissipative eigenmode approach. Neglecting the gas pressure, one readily finds that Equation 15a in TW98 is identical to Equation 21 here. However, our Equation 26 with $g = 1$ seems different from Equation 15b in TW98. This discrepancy is only apparent, and can be reconciled by noting that $\Theta/(1+\Theta) = [1 - \exp(-2k_y R)]/2$. Our Equation 22 therefore generalizes the TW98 results by allowing the TL profile to be as arbitrary as the TB approach allows. Likewise, it generalizes those dissipative eigenmode results where $\Theta \approx 1$ is assumed (Equation 57 in Ruderman, Tirry, and Goossens, 1995, see also the references therein, in particular Mok and Einaudi, 1985; Hollweg and Yang, 1988).

To sum up at this point, the DR (Equation 20) applies to rather arbitrary density profiles, provided $l/R \ll 1$. Furthermore, it is valid for arbitrary values of k_y and k_z . When $k_y^2 \gg |\omega^2/v_A^2|$ and $k_y l \ll 1$, the real part of the eigenfrequency is expressible by Equation 21. Likewise, the imaginary part is given by Equation 22 for general profiles, and specializes to Equation 26 for our profile

choices. However, in the more general situation, Equation 20 needs to be solved numerically after one specifies the parameters in the parantheses in Equation 11. We adopt an iterative approach for this purpose, starting with an initial guess for ω_R such that a temporary value for x_A can be found. We then evaluate the ρ_A/ρ'_A term and solve Equation 20 to yield ω . Adopting this updated ω as a further guess, we iterate this process until it converges to a unique eigenfrequency.

3. Numerical Results

We are now in a position to examine the dispersive properties of resonantly damped kink modes in coronal slabs, for which purpose it is admittedly difficult to exhaust the full parameter space as contained in Equation 11. We choose to present our results in two parts. Section 3.1 will examine how the TB expectations compare with our self-consistent resistive results. On the other hand, section 3.2 will compare different profile specifications regarding their influence on the eigenfrequencies found with the resistive eigenmode approach.

3.1. Comparison of Resistive Computations with Thin-Boundary Expectations

Our examination starts with Figure 3, where the dependencies on the dimensionless TL width (l/R) are shown for both the real part of the eigenfrequency (ω_R , Figure 3a), and the ratio of the imaginary to the real part ($-\omega_I/\omega_R$, Figure 3b). The equilibrium density profile is chosen to be a “sine” one for illustration purposes. Furthermore, the density contrast and the axial wavenumber are fixed at $\rho_i/\rho_e = 10$ and $k_z R = \pi/50$, respectively. Two rather different values of k_y are examined as represented by the curves in different colors. The results from the self-consistent resistive computations are shown by the solid lines. We also solve the explicit DR (Equation 20) in the thin-boundary (TB) limit with both the iterative and analytical approaches, and label the corresponding results with “TB numerical” (the dashed curves) and “TB analytical” (dash-dotted), respectively. Two additional frequencies, $k_z v_{Ai}$ and $\omega_k = k_z c_k$, are also plotted for comparison (see the horizontal ticks in Figure 3a). Examining the TB curves, one sees that the “TB analytical” ones as given by Equations 21 and 26 tend to satisfactorily reproduce the “TB numerical” solutions when $k_y l$ is small, which is evidenced by the close agreement between the black dashed and dash-dotted curves pertaining to $k_y R = 0.25$. This is expected given that $k_y l \ll 1$ is assumed for deriving these expressions and that the additional assumption $k_y^2 \gg |\omega^2/v_A^2|$ tends to hold here. From Figure 3a one also sees that the dash-dotted curves may differ substantially from the kink frequency ω_k when $k_y R$ is not sufficiently large, suggesting the need to incorporate the k_y -dependence in analytical expressions for the eigenfrequency. These details aside, it is more important to note that, relative to the “TB analytical” curves, the “TB numerical” ones tend to deviate more significantly from the resistive results. This happens even though the iterative solution to DR (Equation 20) seems more self-consistent than its analytical counterpart. On top of that, the iterative approach does not converge when

$l/R \gtrsim 1.3$ for $k_y R = 1$, the reason being that ω_R decreases towards $k_z v_{Ai}$ as l/R increases and eventually leaves the Alfvén continuum. While only a “sine” profile is shown, we find that the resistive results tend to agree better with the “TB analytical” rather than the “TB numerical” results for other profiles as well. We therefore conclude that, technically speaking, if one would like to invoke the TB limit to validate the eigenfrequencies numerically found for resonantly damped kink modes in coronal slabs with an equilibrium configuration similar to ours, then it is not worthwhile to further solve the relevant DR numerically. Analytical expressions similar to Equations 21 and 22 serve this purpose better. In what remains, we use ω^{TB} to denote the eigenfrequencies analytically expected with Equations 21 and 26. Likewise, by ω we mean the eigenfrequencies found from resistive computations.

How does ω^{TB} compare with ω if we survey a broader set of parameters? The following definitions are necessary,

$$\delta\omega_R = \frac{2\pi/\omega_R^{\text{TB}}}{2\pi/\omega_R} - 1, \quad \delta(\omega_R/\omega_I) = \frac{\omega_R^{\text{TB}}/\omega_I^{\text{TB}}}{\omega_R/\omega_I} - 1. \quad (30)$$

Evidently, $\delta\omega_R$ and $\delta(\omega_R/\omega_I)$ defined this way pertain to the wave period $P = 2\pi/\omega_R$ and damping-time-to-period ratio $\tau/P = |1/\omega_I|/(2\pi/\omega_R)$, respectively. As such, they essentially comply with the definitions in the cylindrical study by Soler et al. (2014, Equation (10)). The only difference is that we evaluate the relative differences in the algebraic rather than the absolute sense. Negative values of $\delta\omega_R$ or $\delta(\omega_R/\omega_I)$ therefore represent where the TB expectations underestimate the true values of the relevant quantity. In the latter case, this is equivalent to where the TB expectations overestimate the damping rates $[-\omega_I/\omega_R]$.

Figure 4 compares the TB values with the resistive results by showing $\delta\omega_R$ (the left column) and $\delta(\omega_R/\omega_I)$ (right) as functions of the dimensionless TL width l/R and the out-of-plane wavenumber k_y . Here a pair of $[\rho_i/\rho_e, k_z R] = [10, \pi/50]$ is adopted for the density contrast and axial wavenumber. Furthermore, $k_y R$ ranges between 0.02 and 1, and l/R ranges from 0.05 to 1.95. Different profiles are examined in different rows as labeled. The contours in all plots are equally spaced, with negative (positive) values represented by the dotted (solid) curves. One sees that both $\delta\omega_R$ and $\delta(\omega_R/\omega_I)$ show some complicated dependencies on l/R and $k_y R$. Let us first examine the lowermost portions where $k_y R$ is small such that the requirement $k_y^2 \gg |\omega^2/v_A^2|$ is not met for one to arrive at Equations 21 and 26. One sees from the right column that $\delta(\omega_R/\omega_I)$ is consistently positive. While the relevant contours are too crowded to read, a careful inspection indicates that $|\delta(\omega_R/\omega_I)|$ reaches 60%, 110%, and 240% for the sine, linear, and parabolic profiles, respectively. Nonetheless, that $k_y l$ is small in this portion makes it uninteresting in terms of wave damping. More interesting is that the consistently negative $\delta\omega_R$ reaches merely -5.6% , -5.7% , and -10.4% for the sine, linear, and parabolic profiles, respectively.

Now move on to the portions where $k_y \gtrsim k_z$. Inspecting the left column, one sees that $\delta\omega_R$ tends to be positive and increase with l/R or $k_y R$ for the linear and parabolic profiles, peaking at 54% (36%) for the former (latter). The pattern for the sine profile is more complicated, with a positive (negative) maximum of

4.2% (−10.1%) at $[l/R, k_y R] \approx [2, 0.38]$ (close to the upper-right corner). Some profile dependence can also be told for $\delta(\omega_R/\omega_I)$ in the right column. Common to all profiles is that $\delta(\omega_R/\omega_I)$ tends to possess a negative maximum at the upper-right corner, reading −26%, −68%, and −43% for the sine, linear, and parabolic profiles, respectively. Likewise, a positive maximum is attained at $k_y R \approx 1$, reading 20%, 54%, and 8.5% when $l/R \approx 1.39, 0.61$ and 0.82 for the respective profiles. However, a negative maximum exists towards $l/R \approx 2$ for the sine and linear profiles, reaching −15% and −25% when $k_y R \approx 0.26$ and 0.28 . In contrast, for the parabolic profile, the TB expectations show little difference from the resistive results in terms of ω_R/ω_I regardless of l/R when $k_y R$ varies between, say, 0.2 and 0.7.

Figure 5 presents, in a format identical to Figure 4, how $\delta\omega_R$ and $\delta(\omega_R/\omega_I)$ depend on l/R and ρ_i/ρ_e for a fixed pair of $[k_y R, k_z R] = [1, \pi/50]$. The density contrast ρ_i/ρ_e varies between 1.2 and 10, a range that encompasses values representative of both active-region loops (*e.g.* Aschwanden, Nakariakov, and Melnikov, 2004) and streamer stalks (*e.g.* Chen et al., 2011, Figure 2). Furthermore, the dimensionless TL width l/R varies from 0.05 to 1.95. Examining the left column first, one sees that overall $|\delta\omega_R|$ tends to attain its maximum when ρ_i/ρ_e takes the largest value. For the sine profile, $\delta\omega_R$ tends to be negative, peaking at −10.2% when $l \approx 1.43$. However, $\delta\omega_R$ for the rest two profiles tends to be positive, and attains 54% (36%) for the sine (parabolic) one around the upper-right corner. Now move on to the right column. For all profiles, one sees that $\delta(\omega_R/\omega_I)$ for a fixed ρ_i/ρ_e tends to switch from positive to negative values with increasing l/R . The negative maximum for the sine profile is attained at the upper-right corner, the specific value being −26%. However, the corresponding maxima for the linear and parabolic profiles are both attained at the lower-right corner, reading −84% and −71%. On the other hand, $\delta(\omega_R/\omega_I)$ for the sine profile attains a positive maximum of 32% at $[l/R, \rho_i/\rho_e] \approx [1.4, 2.5]$. For comparison, the positive maximum for $\delta(\omega_R/\omega_I)$ attains 55% (8.5%) when $[l/R, \rho_i/\rho_e]$ reads roughly $[0.58, 9]$ ($[0.82, 10]$) for the linear (parabolic) profile.

It proves informative to compare our Figure 5 with its cylindrical counterpart given by Figure 1 in Soler et al. (2014, hereafter S14), thereby highlighting some geometry-related differences in the behavior of resonantly damped kink modes. Two remarks are necessary before proceeding, however. Firstly, as suggested by Goossens, Hollweg, and Sakurai (1992) and Goossens (2008), what we compute for kink modes in a slab geometry can be meaningfully compared with cylindrical results only when $k_y R$ takes integer values as far as the eigenfrequencies are concerned. In particular, if $k_y R$ is specified to be unity, then its cylindrical counterpart is the kink mode. Likewise, integer values of $k_y R$ larger than unity correspond to fluting modes in the cylindrical geometry. Secondly, we note that S14 adopted a value of $k_z R = \pi/100$ for the axial wavenumber, which is slightly different from what we specified. We believe this slight difference is not important for our purpose, because both values of $k_z R$ pertain to the regime where the axial wavelength is much longer than the width of the hosting structure. Nonetheless, we avoid direct comparisons of numeric values in the two geometries.

With the necessary remarks, this comparison can be most readily presented on the basis of individual profiles. For the sine one, the first row in Figure 5

is morphologically different from its cylindrical counterpart (the first row in Figure 1 of S14), where $|\delta\omega_R|$ tends to peak at $[l/R, \rho_i/\rho_e] \approx [2, 6]$ and $|\delta(\omega_R/\omega_I)|$ tends to maximize either when $l/R \approx 1.1$ for large ρ_i/ρ_e or when $l/R \approx 2$ for small ρ_i/ρ_e . Despite this, our slab computations agree with S14 in that the sine profile possesses the least difference between the TB expectations and self-consistently computed eigenfrequencies among the examined profiles. For the linear profile, the second row in Figure 5 is strikingly similar to the second row in Figure 1 of S14. By this we mean that the maxima in $|\delta\omega_R|$ and $|\delta(\omega_R/\omega_I)|$ occur at very similar locations in the $l/R - \rho_i/\rho_e$ plane. For the parabolic profile, a comparison between Figure 5 and Figure 1 of S14 yields that the dependence of $|\delta\omega_R|$ on l/R and ρ_i/ρ_e is remarkably similar in both geometries. However, there is an interesting difference in the behavior of $\delta(\omega_R/\omega_I)$, even though the locations where $|\delta(\omega_R/\omega_I)|$ takes its largest value are similar in the two geometries. For this purpose we focus on the situation where $\rho_i/\rho_e \gtrsim 3$. While $|\delta(\omega_R/\omega_I)|$ is consistently less than 10% for $l/R \lesssim 1$ in the slab case, some rather significant value for $|\delta(\omega_R/\omega_I)|$ arises when l/R exceeds 0.5 in the cylindrical geometry. In physical terms, this means that the TB expectation starts to overestimate the damping rates at some l/R that is substantially larger in the slab than in the cylindrical geometry. We will return to this point later.

3.2. Effects of Profile Specifications on Eigenfrequencies in Resistive Computations

This section focuses on the profile dependence of the eigenfrequencies of resonantly damped kink modes in coronal slabs. For this purpose, we will present only the resistive results. In addition, the density contrast ρ_i/ρ_e is fixed at 10.

We start with Figure 6 where the l/R -dependencies of ω_R (the upper row) and $-\omega_I/\omega_R$ (lower) are compared between the sine and linear (parabolic) profiles in the left (right) column. Different colors are adopted to differentiate different profiles. Likewise, different linestyles pertain to a number of different values for k_y . The combination $[\rho_i/\rho_e, k_z R]$ is fixed at $[10, \pi/50]$. Overall, the point to draw is that the profile specifications are important for determining the eigenfrequencies in general, and the damping rates in particular. Take the first row for instance. For the examined values of k_y , Figure 6a indicates that the differences in ω_R between the sine and linear profiles tend to increase with k_y , which is particularly true for thick TLs. When $k_y R = 1$, the two profiles can hardly be distinguished in terms of ω_R for $l/R \lesssim 0.5$. At larger l/R , however, ω_R for the sine profile gradually decreases to some minimum at $l/R \approx 1.4$ and then increases. In contrast, ω_R for the linear profile increases monotonically, eventually exceeding its sine counterpart by 66% when $l/R \approx 2$. Moving on to Figure 6b, one sees that ω_R for the parabolic profile tends to be smaller than for the sine one when $k_y R \lesssim 0.5$, with the tendency reversed for larger values of $k_y R$. When $k_y R = 1$, the values of ω_R may differ substantially between the two profiles, with the parabolic one exceeding the sine one by 48% for $l/R \approx 2$. Now let us examine the second row. A comparison of Figure 6c with 6d indicates that in general the differences in $-\omega_I/\omega_R$ between the sine and linear profiles are more significant than those between the sine and parabolic profiles. For sufficiently

small l/R , this behavior is understandable given the profile dependence of the factor g in Equation 26. Focusing on the case where $k_y R = 1$, one readily finds that g evaluates to 0.64 and 0.66 for the sine and parabolic profiles, respectively. These values are substantially different from unity, the value that g takes up for the linear profile. The dash-dotted curves in Figure 6d indicate that the linear l/R -dependence expected in the TB limit persists until $l/R \lesssim 1$ for the sine and parabolic profiles. However, $-\omega_I/\omega_R$ for the linear profile starts to deviate from the TB behavior at considerably smaller l/R . In fact, the red dash-dotted curve in Figure 6c suggests that $-\omega_I/\omega_R$ reaches some maximum around $l/R \gtrsim 0.6$ and then decreases with l/R . As a result, the values that $-\omega_I/\omega_R$ attain at $l/R \gtrsim 0.6$ for the linear profile may exceed those for the sine one by as much as 126%.

With Figure 6 we further remark on the similarities and differences in the eigenfrequencies of resonantly damped kink modes between the slab and cylindrical geometries. We examine only the linear and parabolic profiles for this purpose, given the difficulty to exhaust the comparison between the geometries. In addition, we focus on the case $k_y R = 1$ such that this comparison is meaningful. For the linear one, we note that the l/R -dependencies of ω_R and $-\omega_I/\omega_R$ are qualitatively similar to their cylindrical counterpart as given by Figure 5 in Soler et al. (2013, S13). In particular, the values of ω_R in both geometries nearly stay constant at small l/R but then increase substantially with l/R . Likewise, a nonmonotonical l/R -dependence of $-\omega_I$ is common to both geometries. While not shown, the plot of ω_I rather than $-\omega_I/\omega_R$ is remarkably similar to Figure 5 in S13. We also note that this behavior of the eigenfrequencies was originally found in the slab computations by TW98 to our knowledge. It is worth noting that this remarkable similarity is found even though S13 employed a different combination $[\rho_i/\rho_e, k_z R]$ of $[5, \pi/100]$. The comparison of the parabolic results between the two geometries is interesting from another perspective, for which purpose we note that the horizontal dashed lines in the lower row in Figure 6 represent $1/2\pi$. Evidently, this corresponds to the situation where the ratio of the damping time to period reaches unity, which may serve as a dividing line separating the under-damped from over-damped modes. As implied by Figure 5 in S13 and further corroborated by Figure 1 in S14, kink modes in the cylindrical geometry can hardly become over-damped. This happens because while the TB expressions readily predict over-damping for sufficiently large l/R , the actual values of $-\omega_I/\omega_R$ at those values of l/R are smaller than the TB expectations. In the slab geometry, however, the l/R -dependence of $-\omega_I/\omega_R$ starts to deviate from the TB expectations only when $l/R \gtrsim 1$. For comparison, Equation 26 predicts that $-\omega_I/\omega_R$ exceeds $1/2\pi$ when $l/R \geq 0.78$. As a result, the blue dash-dotted curve in Figure 6d stays above the horizontal line for $l/R \gtrsim 0.72$, and peaks at 0.25 despite that the curve decreases with l/R eventually. We note by passing that fluting modes in the cylindrical geometry can readily become over-damped by resonant absorption in the Alfvén continuum (Soler, 2017).

Distinguishing the over-damped from under-damped situations can also help bring out the profile dependence. Looking at the lower row in Figure 6 and specializing to a profile, at a given k_y we can deduce a critical TL width $(l/R)_{\text{crit}}$ beyond which $-\omega_I/\omega_R$ starts to exceed $1/2\pi$. Surveying a more extensive range

of k_y then leads to Figure 7, where $(l/R)_{\text{crit}}$ is plotted as a function of k_y in different colors for different profile choices. One sees that the curves labeled “sine” and “parabolic” are close to one another, understandable given the insignificant differences in $-\omega_I/\omega_R$ between the two profiles at sufficiently small l/R . However, these two curves deviate considerably from the curve labeled “linear”, which is true throughout the entire range of k_y examined here.

The computations so far correspond to a fixed axial wavenumber of $k_z R = \pi/50$, which is more relevant for standing kink modes trapped in, say, AR loops or AR arcades. However, examining other values of k_z will be informative to say the least, and we look back at the parameters in the parentheses in Equation 11 for this purpose. If we allow only k_y to vary and construct a plot similar to Figure 6b, then we end up with a critical $k_{y,\text{crit}}$ that corresponds to $-\omega_I/\omega_R = 1/2\pi$. Further varying k_z therefore leads to a series of $k_{y,\text{crit}}$, and the output from such a practice with $l/R = 0.5$ is plotted in Figure 8. Here different density profiles are represented by the solid curves in different colors. When placed in the k_y - k_z plane, the under-damped (over-damped) modes then lie below (above) the relevant solid curve for a specific profile prescription. Above all, one sees once again the importance of profile prescriptions for determining the dispersive properties of resonantly damped modes. When examined this way, not only does the curve labeled “linear” lie at quite some distance away from the rest, but also some substantial difference arises between the curves labeled “sine” and “parabolic”.

Figure 8 allows us to say a few words on impulsively generated kink waves in coronal slabs, in which context streamer waves are likely to be relevant. Suppose that these waves result from the lateral impingement on a coronal slab by, say, a bulk of mass (coronal mass ejections in the case of streamer waves, see, *e.g.* Chen et al., 2010; Feng et al., 2011; Decraemer, Zhukov, and Van Doorselaere, 2020). It seems observationally difficult to tell the characteristics of the interaction between the slab and, say, the mass motion. To make some quantitative progress, we nonetheless assume that the duration of the interaction is shorter than the (quasi-)periods of the resulting waves. We further assume that the interaction is spatially isotropic in the x - y plane (see Figure 1a) and specifically possesses a Gaussian form $\exp[-(x^2 + y^2)/2\Delta^2]$. Evidently, Δ measures the spatial extent of the interaction. The power spectral density (PSD) is then $\propto \exp[-(k_y^2 + k_z^2)\Delta^2]$, and therefore decreases from its maximum by a factor of e along a circle of radius $1/\Delta$ in the k_y - k_z plane. The dashed circles in Figure 8 correspond to a series of Δ uniformly spaced by R , with the outermost one corresponding to $\Delta = R$. Two situations then arise regarding the damping of the components constituting an impulsive wave. If $\Delta \gtrsim 2R$, then the majority of the components can survive resonant damping. If $\Delta \lesssim R$ instead, then the heavy resonant damping of the components pertaining to the upper-left corner in Figure 8 will make it difficult for them to propagate to large distances. While these statements are enabled by Figure 8, this figure alone does not allow us to tell the eventual temporal and spatial variations of impulsively generated waves. To name but one intricacy, we note that wave dispersion is well known to play a critical role in the dynamics of impulsive waves in both cylindrical (*e.g.* Roberts, Edwin, and Benz, 1983; Edwin and Roberts, 1986; Oliver, Ruderman, and Terradas, 2014, 2015; Shestov,

Nakariakov, and Kuzin, 2015; Yu et al., 2016, 2017) and Cartesian equilibria (*e.g.* Edwin, Roberts, and Hughes, 1986; Murawski and Roberts, 1993; Nakariakov et al., 2004; Pascoe, Nakariakov, and Kupriyanova, 2013; Yu, Nakariakov, and Yan, 2016; Li et al., 2018; Goddard, Nakariakov, and Pascoe, 2019). Of particular relevance is the one by Murawski and Roberts (1993), who performed two-dimensional (2D) time-dependent simulations to examine the response of a coronal slab to a lateral exciter. An extension of this study to 3D will clarify the behavior of the impulsively generated waves when the spatial extent of the driver is finite in the y -direction. Consequently, our eigenmode analysis involving a finite k_y will be much relevant, as we have practiced previously in other contexts (*e.g.* Yu et al., 2017; Li et al., 2018).

4. Summary

This study was motivated by the apparent lack of an extensive survey of the parameters that may influence the resonant damping of kink modes in straight coronal slabs. To this end, we worked in the framework of pressure-less, gravity-free, resistive MHD and adopted an eigenvalue problem (EVP) approach. The equilibrium density was restricted to be structured only in the x -direction, but was allowed to take a rather generic form comprising a uniform interior, a uniform exterior, and a continuous transition layer (TL) in between. Inspired by examinations on resonantly damped kink modes in coronal cylinders (Soler et al., 2013, 2014), we paid special attention to the effects of the mathematical form for describing the density profile (“profile” for brevity). By doing this we generalized the study by Arregui et al. (2007a), who addressed an identical problem but nonetheless took a particular profile and examined only the influence of the out-of-plane wavenumber k_y . We additionally conducted an analytical study in the thin-boundary (TB) limit, and the resulting expressions generalized previous results by allowing a broader set of profile choices and/or a broader range of k_y .

Our results are summarized as follows: Technically speaking, we find that the eigenfrequencies computed with the self-consistent resistive approach tend to agree better with the analytical rather than the numerical solutions to the dispersion relation (Equation 20) derived in the TB limit. We therefore recommend expressions similar to Equations 21 and 22 for one to validate numerical studies on resonantly damped kink modes in an equilibrium similar to ours. Physically speaking, we find that the eigenfrequencies in general, and the damping efficiency in particular, are sensitive to how the density profile is formulated. In particular, the ratio of the imaginary to the real part of the eigenfrequency for the linear profile can readily exceed its sine counterpart by a factor of two or so. When quantifying the deviation of the self-consistently computed eigenfrequencies from the TB expectations, we highlighted some differences in resonantly damped kink modes between the slab and cylindrical geometries. An exemplary result pertains to the parabolic profile, for which we find that kink modes in the slab (cylindrical) case can readily (hardly) become over-damped. We also connected our computations to impulsively generated kink waves in coronal slabs by assuming that the impulsive driver depends on x - y in a Gaussian form characterized by a

spatial scale Δ . In the parameter range that we examined, we find that resonant absorption becomes relevant when $\Delta \lesssim R$, strongly damping those components with $k_y \gtrsim 1/R$ where R is the slab half-width.

Coronal structures are admittedly far more complicated than modeled here, in which context we name only two intricacies before closing: First, it proves observationally difficult to tell the mathematical form for the density profile, one primary culprit being that the corona is optically thin in, say, the EUV. Seeing coronal loops as cylinders, one way to tackle this issue has been to experiment with a number of profiles and contrast the forward-modeled EUV intensities with measurements by, say, TRACE (*e.g.* Aschwanden et al., 2003) or the Atmospheric Imaging Assembly on board the Solar Dynamics Observatory (SDO/AIA, *e.g.* Pascoe et al., 2017). However, while there is strong evidence that the density distribution is continuous rather than discontinuous, a statistical survey indicates that it is difficult to further discriminate between different profiles (Goddard et al., 2017). On this aspect we note that evidence-based model comparison in the Bayesian framework is a promising way forward (*e.g.* Arregui, Soler, and Asensio Ramos, 2015; Anfinogentov et al., 2021, see also the review by Arregui, 2018). Second, structural curvature needs to be accounted for when oscillations in, say, active-region arcades are examined. A step forward is to consider a cylindrical system (r, θ, y) and assume that the equilibrium magnetic field \mathbf{B}_0 is of the form $\hat{\theta}/r$. When $k_y \neq 0$, resonant absorption was shown to remain relevant by Hindman and Jain (2018), who nonetheless assumed a particular density profile to ensure that kink modes are trapped. For other profiles, however, lateral leakage is in general operational (*e.g.* Verwichte, Foullon, and Nakariakov, 2006; Díaz, Zaqarashvili, and Roberts, 2006), even though this effect tends to weaken with k_y (Rial et al., 2013). We take these intricacies as strengthening rather than weakening the need for further examinations of coronal kink modes in a slab configuration. Regarding the first intricacy, that the eigenfrequencies are sensitive to profile choices can be employed in conjunction with the forward-modeling approach to tighten the constraints on the profile description, as has been practiced by Pascoe et al. (2018), who adopted a cylindrical geometry. Likewise, the second intricacy means that a systematic study is needed to assess the importance of resonant absorption relative to lateral leakage for kink modes in curved slabs, which has been initiated by Rial et al. (2013). All of these developments are warranted, but nonetheless are left for future studies.

Acknowledgments We thank the referee for his/her constructive comments, which helped improve the manuscript substantially. This research was supported by the National Natural Science Foundation of China (HY:41704165, BL: 41674172, 11761141002, 41974200; SX:41604145) and by Shandong University via grant No 2017JQ07. We also acknowledge the International Space Science Institute-Beijing (ISSI-BJ) for supporting the international teams “MHD Seismology of the Solar Corona” and “Pulsations in solar flares: matching observations and models”.

Disclosure of Potential Conflicts of Interest The authors declare that they have no conflicts of interest.

References

- Allcock, M., Erdélyi, R.: 2017, Magnetohydrodynamic Waves in an Asymmetric Magnetic Slab. *Solar Phys.* **292**, 35. DOI. ADS.
- Allian, F., Jain, R., Hindman, B.W.: 2019, A New Analysis Procedure for Detecting Periodicities within Complex Solar Coronal Arcades. *Astrophys. J.* **880**, 3. DOI. ADS.
- Andries, J., Tirry, W.J., Goossens, M.: 2000, Modified Kelvin-Helmholtz Instabilities and Resonant Flow Instabilities in a One-dimensional Coronal Plume Model: Results for Plasma $\beta=0$. *Astrophys. J.* **531**, 561. DOI. ADS.
- Anfinogentov, S.A., Nakariakov, V.M.: 2019, Magnetohydrodynamic Seismology of Quiet Solar Active Regions. *Astrophys. J. Lett.* **884**, L40. DOI. ADS.
- Anfinogentov, S.A., Nakariakov, V.M., Pascoe, D.J., Goddard, C.R.: 2021, Solar Bayesian Analysis Toolkit—A New Markov Chain Monte Carlo IDL Code for Bayesian Parameter Inference. *Astrophys. J. Suppl. Series* **252**, 11. DOI. ADS.
- Arregui, I.: 2015, Wave heating of the solar atmosphere. *Philosophical Transactions of the Royal Society of London Series A* **373**, 20140261. DOI. ADS.
- Arregui, I.: 2018, Bayesian coronal seismology. *Advances in Space Research* **61**, 655. DOI. ADS.
- Arregui, I., Asensio Ramos, A.: 2014, Determination of the cross-field density structuring in coronal waveguides using the damping of transverse waves. *Astron. Astrophys.* **565**, A78. DOI. ADS.
- Arregui, I., Goossens, M.: 2019, No unique solution to the seismological problem of standing kink magnetohydrodynamic waves. *Astron. Astrophys.* **622**, A44. DOI. ADS.
- Arregui, I., Soler, R., Asensio Ramos, A.: 2015, Model Comparison for the Density Structure across Solar Coronal Waveguides. *Astrophys. J.* **811**, 104. DOI. ADS.
- Arregui, I., Terradas, J., Oliver, R., Ballester, J.L.: 2007a, Resonantly Damped Surface and Body MHD Waves in a Solar Coronal Slab with Oblique Propagation. *Solar Phys.* **246**, 213. DOI. ADS.
- Arregui, I., Terradas, J., Oliver, R., Ballester, J.L.: 2007b, The influence of the internal structuring of coronal loops on the properties of their damped transverse oscillations. *Astron. Astrophys.* **466**, 1145. DOI. ADS.
- Aschwanden, M.J., Nakariakov, V.M., Melnikov, V.F.: 2004, Magnetohydrodynamic Sausage-Mode Oscillations in Coronal Loops. *Astrophys. J.* **600**, 458. DOI. ADS.
- Aschwanden, M.J., Fletcher, L., Schrijver, C.J., Alexander, D.: 1999, Coronal Loop Oscillations Observed with the Transition Region and Coronal Explorer. *Astrophys. J.* **520**, 880. DOI. ADS.
- Aschwanden, M.J., Nightingale, R.W., Andries, J., Goossens, M., Van Doorselaere, T.: 2003, Observational Tests of Damping by Resonant Absorption in Coronal Loop Oscillations. *Astrophys. J.* **598**, 1375. DOI. ADS.
- Ballester, J.L., Erdélyi, R., Hood, A.W., Leibacher, J.W., Nakariakov, V.M.: 2007, Preface: A Topical Issue in Honor of Professor Bernard Roberts. *Solar Phys.* **246**, 1. DOI. ADS.
- Cally, P.S.: 1986, Leaky and Non-Leaky Oscillations in Magnetic Flux Tubes. *Solar Phys.* **103**, 277. DOI. ADS.
- Chen, L., Hasegawa, A.: 1974, Plasma heating by spatial resonance of Alfvén wave. *Physics of Fluids* **17**, 1399. DOI. ADS.
- Chen, S.-X., Li, B., Shi, M., Yu, H.: 2018a, Damping of Slow Surface Sausage Modes in Photospheric Waveguides. *Astrophys. J.* **868**, 5. DOI. ADS.
- Chen, S.-X., Li, B., Kumar, S., Yu, H., Shi, M.: 2018b, Fast Standing Modes in Transversely Nonuniform Solar Coronal Slabs: The Effects of a Finite Plasma Beta. *Astrophys. J.* **855**, 47. DOI. ADS.
- Chen, S.-X., Li, B., Van Doorselaere, T., Goossens, M., Yu, H., Geeraerts, M.: 2021, Damping of Slow Surface Kink Modes in Solar Photospheric Waveguides Modeled by One-dimensional Inhomogeneities. *Astrophys. J.* **908**, 230. DOI. ADS.
- Chen, Y., Song, H.Q., Li, B., Xia, L.D., Wu, Z., Fu, H., Li, X.: 2010, Streamer Waves Driven by Coronal Mass Ejections. *Astrophys. J.* **714**, 644. DOI. ADS.
- Chen, Y., Feng, S.W., Li, B., Song, H.Q., Xia, L.D., Kong, X.L., Li, X.: 2011, A Coronal Seismological Study with Streamer Waves. *Astrophys. J.* **728**, 147. DOI. ADS.
- Cranmer, S.R., Winebarger, A.R.: 2019, The Properties of the Solar Corona and Its Connection to the Solar Wind. *Annu. Rev. Astron. Astrophys.* **57**, 157. DOI. ADS.

- De Moortel, I., Nakariakov, V.M.: 2012, Magnetohydrodynamic waves and coronal seismology: an overview of recent results. *Philosophical Transactions of the Royal Society of London Series A* **370**, 3193. DOI. ADS.
- Decraemer, B., Zhukov, A.N., Van Doorselaere, T.: 2019, Three-dimensional Density Structure of a Solar Coronal Streamer Observed by SOHO/LASCO and STEREO/COR2 in Quadrature. *Astrophys. J.* **883**, 152. DOI. ADS.
- Decraemer, B., Zhukov, A.N., Van Doorselaere, T.: 2020, Properties of Streamer Wave Events Observed during the STEREO Era. *Astrophys. J.* **893**, 78. DOI. ADS.
- Díaz, A.J., Zaqarashvili, T., Roberts, B.: 2006, Fast magnetohydrodynamic oscillations in a force-free line-tied coronal arcade. *Astron. Astrophys.* **455**, 709. DOI. ADS.
- Edwin, P.M., Roberts, B.: 1982, Wave Propagation in a Magnetically Structured Atmosphere - Part Three - the Slab in a Magnetic Environment. *Solar Phys.* **76**, 239. DOI. ADS.
- Edwin, P.M., Roberts, B.: 1983, Wave Propagation in a Magnetic Cylinder. *Solar Phys.* **88**, 179. DOI. ADS.
- Edwin, P.M., Roberts, B.: 1986, Impulsively generated fast coronal pulsations. In: *NASA Conference Publication, NASA Conference Publication* **2449**, 347. ADS.
- Edwin, P.M., Roberts, B.: 1988, Employing analogies for ducted MHD waves in dense coronal structures. *Astron. Astrophys.* **192**, 343. ADS.
- Edwin, P.M., Roberts, B., Hughes, W.J.: 1986, Dispersive ducting of MHD waves in the plasma sheet: A source of Pi2 wave bursts. *Geophys. Res. Lett.* **13**, 373. DOI. ADS.
- Erdélyi, R., Goossens, M.: 2011, Magnetohydrodynamic Waves and Seismology of the Solar Atmosphere. *Space Sci. Rev.* **158**, 167. DOI. ADS.
- Feng, S.W., Chen, Y., Li, B., Song, H.Q., Kong, X.L., Xia, L.D., Feng, X.S.: 2011, Streamer Wave Events Observed in Solar Cycle 23. *Solar Phys.* **272**, 119. DOI. ADS.
- Goddard, C.R., Nakariakov, V.M., Pascoe, D.J.: 2019, Fast magnetoacoustic wave trains with time-dependent drivers. *Astron. Astrophys.* **624**, L4. DOI. ADS.
- Goddard, C.R., Pascoe, D.J., Anfinogentov, S., Nakariakov, V.M.: 2017, A statistical study of the inferred transverse density profile of coronal loop threads observed with SDO/AIA. *Astron. Astrophys.* **605**, A65. DOI. ADS.
- Goossens, M.: 2008, Seismology of kink oscillations in coronal loops: Two decades of resonant damping. In: Erdélyi, R., Mendoza-Briceno, C.A. (eds.) *Waves & Oscillations in the Solar Atmosphere: Heating and Magneto-Seismology* **247**, 228. DOI. ADS.
- Goossens, M., Andries, J., Aschwanden, M.J.: 2002, Coronal loop oscillations. An interpretation in terms of resonant absorption of quasi-mode kink oscillations. *Astron. Astrophys.* **394**, L39. DOI. ADS.
- Goossens, M., Erdélyi, R., Ruderman, M.S.: 2011, Resonant MHD Waves in the Solar Atmosphere. *Space Sci. Rev.* **158**, 289. DOI. ADS.
- Goossens, M., Hollweg, J.V., Sakurai, T.: 1992, Resonant Behaviour of Magnetohydrodynamic Waves on Magnetic Flux Tubes - Part Three. *Solar Phys.* **138**, 233. DOI. ADS.
- Goossens, M., Arregui, I., Ballester, J.L., Wang, T.J.: 2008, Analytic approximate seismology of transversely oscillating coronal loops. *Astron. Astrophys.* **484**, 851. DOI. ADS.
- Grossmann, W., Tataronis, J.: 1973, Decay of MHD waves by phase mixing. *Zeitschrift für Physik* **261**, 217. DOI. ADS.
- Guo, M.-Z., Chen, S.-X., Li, B., Xia, L.-D., Yu, H.: 2016, Inferring Flare Loop Parameters with Measurements of Standing Sausage Modes. *Solar Phys.* **291**, 877. DOI. ADS.
- Hasegawa, A., Chen, L.: 1974, Plasma Heating by Alfvén-Wave Phase Mixing. *Phys. Rev. Lett.* **32**, 454. DOI. ADS.
- Hindman, B.W., Jain, R.: 2018, A Novel Approach to Resonant Absorption of the Fast Magnetohydrodynamic Eigenmodes of a Coronal Arcade. *Astrophys. J.* **858**, 6. DOI. ADS.
- Hollweg, J.V., Yang, G.: 1988, Resonance absorption of compressible magnetohydrodynamic waves at thin “surfaces”. *J. Geophys. Res.* **93**, 5423. DOI. ADS.
- Hornsey, C., Nakariakov, V.M., Fludra, A.: 2014, Sausage oscillations of coronal plasma slabs. *Astron. Astrophys.* **567**, A24. DOI. ADS.
- Ionson, J.A.: 1978, Resonant absorption of Alfvénic surface waves and the heating of solar coronal loops. *Astrophys. J.* **226**, 650. DOI. ADS.
- Jain, R., Maurya, R.A., Hindman, B.W.: 2015, Fundamental-mode Oscillations of Two Coronal Loops within a Solar Magnetic Arcade. *Astrophys. J. Lett.* **804**, L19. DOI. ADS.
- Kwon, R.-Y., Ofman, L., Olmedo, O., Kramar, M., Davila, J.M., Thompson, B.J., Cho, K.-S.: 2013, STEREO Observations of Fast Magnetosonic Waves in the Extended Solar Corona Associated with EIT/EUV Waves. *Astrophys. J.* **766**, 55. DOI. ADS.

- Li, B., Guo, M.-Z., Yu, H., Chen, S.-X.: 2018, Impulsively Generated Wave Trains in Coronal Structures. II. Effects of Transverse Structuring on Sausage Waves in Pressureless Slabs. *Astrophys. J.* **855**, 53. DOI. ADS.
- Li, B., Antolin, P., Guo, M.-Z., Kuznetsov, A.A., Pascoe, D.J., Van Doorselaere, T., Vasheghani Farahani, S.: 2020, Magnetohydrodynamic Fast Sausage Waves in the Solar Corona. *Space Sci. Rev.* **216**, 136. DOI. ADS.
- Lopin, I., Nagorny, I.: 2015, Sausage Waves in Transversely Nonuniform Monolithic Coronal Tubes. *Astrophys. J.* **810**, 87. DOI. ADS.
- Mok, Y., Einaudi, G.: 1985, Resistive decay of Alfvén waves in a non-uniform plasma. *Journal of Plasma Physics* **33**, 199. DOI. ADS.
- Murawski, K., Roberts, B.: 1993, Numerical Simulations of Fast Magnetohydrodynamic Waves in a Coronal Plasma - Part Two. *Solar Phys.* **144**, 101. DOI. ADS.
- Nakariakov, V.M., Erdélyi, R.: 2009, Foreword. *Space Sci. Rev.* **149**, 1. DOI. ADS.
- Nakariakov, V.M., Kolotkov, D.Y.: 2020, Magnetohydrodynamic Waves in the Solar Corona. *Annu. Rev. Astron. Astrophys.* **58**, 441. DOI. ADS.
- Nakariakov, V.M., Ofman, L.: 2001, Determination of the coronal magnetic field by coronal loop oscillations. *Astron. Astrophys.* **372**, L53. DOI. ADS.
- Nakariakov, V.M., Ofman, L., Deluca, E.E., Roberts, B., Davila, J.M.: 1999, TRACE observation of damped coronal loop oscillations: Implications for coronal heating. *Science* **285**, 862. DOI. ADS.
- Nakariakov, V.M., Arber, T.D., Ault, C.E., Katsiyannis, A.C., Williams, D.R., Keenan, F.P.: 2004, Time signatures of impulsively generated coronal fast wave trains. *Mon. Not. Roy. Astron. Soc.* **349**, 705. DOI. ADS.
- Nakariakov, V.M., Pilipenko, V., Heilig, B., Jelínek, P., Karlický, M., Klimushkin, D.Y., Kolotkov, D.Y., Lee, D.-H., Nisticò, G., Van Doorselaere, T., Verth, G., Zimovets, I.V.: 2016, Magnetohydrodynamic Oscillations in the Solar Corona and Earth's Magnetosphere: Towards Consolidated Understanding. *Space Sci. Rev.* **200**, 75. DOI. ADS.
- Oliver, R., Ruderman, M.S., Terradas, J.: 2014, Propagation and Dispersion of Transverse Wave Trains in Magnetic Flux Tubes. *Astrophys. J.* **789**, 48. DOI. ADS.
- Oliver, R., Ruderman, M.S., Terradas, J.: 2015, Propagation and Dispersion of Sausage Wave Trains in Magnetic Flux Tubes. *Astrophys. J.* **806**, 56. DOI. ADS.
- Oxley, W., Zsámberger, N.K., Erdélyi, R.: 2020, Standing MHD Waves in a Magnetic Slab Embedded in an Asymmetric Magnetic Plasma Environment: Surface Waves. *Astrophys. J.* **898**, 19. DOI. ADS.
- Pascoe, D.J., Nakariakov, V.M., Kupriyanova, E.G.: 2013, Fast magnetoacoustic wave trains in magnetic funnels of the solar corona. *Astron. Astrophys.* **560**, A97. DOI. ADS.
- Pascoe, D.J., Goddard, C.R., Anfinogentov, S., Nakariakov, V.M.: 2017, Coronal loop density profile estimated by forward modelling of EUV intensity. *Astron. Astrophys.* **600**, L7. DOI. ADS.
- Pascoe, D.J., Anfinogentov, S.A., Goddard, C.R., Nakariakov, V.M.: 2018, Spatiotemporal Analysis of Coronal Loops Using Seismology of Damped Kink Oscillations and Forward Modeling of EUV Intensity Profiles. *Astrophys. J.* **860**, 31. DOI. ADS.
- Poedts, S., Kerner, W.: 1991, Ideal quasimodes reviewed in resistive magnetohydrodynamics. *Phys. Rev. Lett.* **66**, 2871. DOI. ADS.
- Rial, S., Arregui, I., Terradas, J., Oliver, R., Ballester, J.L.: 2013, Wave Leakage and Resonant Absorption in a Loop Embedded in a Coronal Arcade. *Astrophys. J.* **763**, 16. DOI. ADS.
- Roberts, B.: 2019, *Mhd waves in the solar atmosphere*, Cambridge University Press. DOI.
- Roberts, B., Edwin, P.M., Benz, A.O.: 1983, Fast pulsations in the solar corona. *Nature* **305**, 688. DOI. ADS.
- Rosenberg, H.: 1970, Evidence for MHD Pulsations in the Solar Corona. *Astron. Astrophys.* **9**, 159. ADS.
- Ruderman, M.S., Roberts, B.: 2002, The Damping of Coronal Loop Oscillations. *Astrophys. J.* **577**, 475. DOI. ADS.
- Ruderman, M.S., Tirry, W., Goossens, M.: 1995, Non-stationary resonant Alfvén surface waves in one-dimensional magnetic plasmas. *Journal of Plasma Physics* **54**, 129. DOI. ADS.
- Sakurai, T., Goossens, M., Hollweg, J.V.: 1991, Resonant Behaviour of Magnetohydrodynamic Waves on Magnetic Flux Tubes - Part One. *Solar Phys.* **133**, 227. DOI. ADS.
- Sewell, G.: 1988, *The Numerical Solution of Ordinary and Partial Differential Equations*, San Diego: Academic Press.

- Shestov, S., Nakariakov, V.M., Kuzin, S.: 2015, Fast Magnetoacoustic Wave Trains of Sausage Symmetry in Cylindrical Waveguides of the Solar Corona. *Astrophys. J.* **814**, 135. DOI. ADS.
- Soler, R.: 2017, Fluting Modes in Transversely Nonuniform Solar Flux Tubes. *Astrophys. J.* **850**, 114. DOI. ADS.
- Soler, R., Oliver, R., Ballester, J.L., Goossens, M.: 2009, Damping of Filament Thread Oscillations: Effect of the Slow Continuum. *Astrophys. J. Lett.* **695**, L166. DOI. ADS.
- Soler, R., Goossens, M., Terradas, J., Oliver, R.: 2013, The Behavior of Transverse Waves in Nonuniform Solar Flux Tubes. I. Comparison of Ideal and Resistive Results. *Astrophys. J.* **777**, 158. DOI. ADS.
- Soler, R., Goossens, M., Terradas, J., Oliver, R.: 2014, The Behavior of Transverse Waves in Nonuniform Solar Flux Tubes. II. Implications for Coronal Loop Seismology. *Astrophys. J.* **781**, 111. DOI. ADS.
- Spruit, H.C.: 1982, Propagation Speeds and Acoustic Damping of Waves in Magnetic Flux Tubes. *Solar Phys.* **75**, 3. DOI. ADS.
- Tataronis, J., Grossmann, W.: 1973, Decay of MHD waves by phase mixing. *Zeitschrift fur Physik* **261**, 203. DOI. ADS.
- Tatsuno, T., Wakatani, M.: 1998, Damping of Surface Alfvén Wave in a Slab Plasma. *Journal of the Physical Society of Japan* **67**, 2322. DOI. ADS.
- Terradas, J., Oliver, R., Ballester, J.L.: 2006, Damped Coronal Loop Oscillations: Time-dependent Results. *Astrophys. J.* **642**, 533. DOI. ADS.
- Tirry, W.J., Goossens, M.: 1996, Quasi-Modes as Dissipative Magnetohydrodynamic Eigenmodes: Results for One-dimensional Equilibrium States. *Astrophys. J.* **471**, 501. DOI. ADS.
- Van Doorselaere, T., Andries, J., Poedts, S., Goossens, M.: 2004, Damping of Coronal Loop Oscillations: Calculation of Resonantly Damped Kink Oscillations of One-dimensional Nonuniform Loops. *Astrophys. J.* **606**, 1223. DOI. ADS.
- Van Doorselaere, T., Srivastava, A.K., Antolin, P., Magyar, N., Vasheghani Farahani, S., Tian, H., Kolotkov, D., Ofman, L., Guo, M., Arregui, I., De Moortel, I., Pascoe, D.: 2020a, Coronal Heating by MHD Waves. *Space Sci. Rev.* **216**, 140. DOI. ADS.
- Van Doorselaere, T., Nakariakov, V.M., Li, B., Antolin, P.: 2020b, Editorial: Magnetohydrodynamic Waves in the Solar Atmosphere: Heating and Seismology. *Frontiers in Astronomy and Space Sciences* **6**, 79. DOI. ADS.
- Verwichte, E., Foullon, C., Nakariakov, V.M.: 2006, Fast magnetoacoustic waves in curved coronal loops. *Astron. Astrophys.* **446**, 1139. DOI. ADS.
- Verwichte, E., Nakariakov, V.M., Cooper, F.C.: 2005, Transverse waves in a post-flare supracarade. *Astron. Astrophys.* **430**, L65. DOI. ADS.
- Wang, T., Ofman, L., Yuan, D., Reale, F., Kolotkov, D.Y., Srivastava, A.K.: 2021, Slow-Mode Magnetoacoustic Waves in Coronal Loops. *Space Sci. Rev.* **217**, 34. DOI. ADS.
- Wentzel, D.G.: 1979a, Hydromagnetic surface waves. *Astrophys. J.* **227**, 319. DOI. ADS.
- Wentzel, D.G.: 1979b, The dissipation of hydromagnetic surface waves. *Astrophys. J.* **233**, 756. DOI. ADS.
- Yang, Z., Bethge, C., Tian, H., Tomczyk, S., Morton, R., Del Zanna, G., McIntosh, S.W., Karak, B.B., Gibson, S., Samanta, T., He, J., Chen, Y., Wang, L.: 2020, Global maps of the magnetic field in the solar corona. *Science* **369**, 694. DOI. ADS.
- Yu, H., Li, B., Chen, S.-X., Guo, M.-Z.: 2015, Kink and Sausage Modes in Nonuniform Magnetic Slabs with Continuous Transverse Density Distributions. *Astrophys. J.* **814**, 60. DOI. ADS.
- Yu, H., Li, B., Chen, S.-X., Xiong, M., Guo, M.-Z.: 2016, Impulsively Generated Sausage Waves in Coronal Tubes with Transversally Continuous Structuring. *Astrophys. J.* **833**, 51. DOI. ADS.
- Yu, H., Li, B., Chen, S.-X., Xiong, M., Guo, M.-Z.: 2017, Impulsively Generated Wave Trains in Coronal Structures. I. Effects of Transverse Structuring on Sausage Waves in Pressureless Tubes. *Astrophys. J.* **836**, 1. DOI. ADS.
- Yu, S., Nakariakov, V.M., Yan, Y.: 2016, Effect of a Sausage Oscillation on Radio Zebra-pattern Structures in a Solar Flare. *Astrophys. J.* **826**, 78. DOI. ADS.
- Zajtsev, V.V., Stepanov, A.V.: 1975, On the origin of pulsations of type IV solar radio emission. Plasma cylinder oscillations (I). *Issledovaniia Geomagnetizmu Aeronomii i Fizike Solntsa* **37**, 3. ADS.

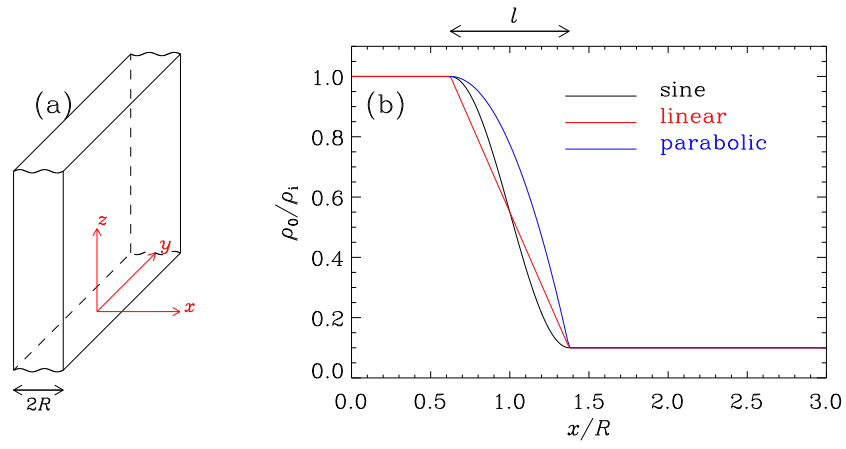


Figure 1. (a) Schematic illustration of the equilibrium configuration, and (b) transverse distributions of the equilibrium density ρ_0 . All density profiles are characterized by a transition layer (TL) that continuously connects a uniform interior to a uniform exterior. This TL is located between $x_i = R - l/2$ and $x_e = R + l/2$, where R is the mean slab half-width and l the TL width. For illustration purposes, the density contrast $[\rho_i/\rho_e]$ and the dimensionless TL width $[l/R]$ are chosen to be 10 and 0.75, respectively.

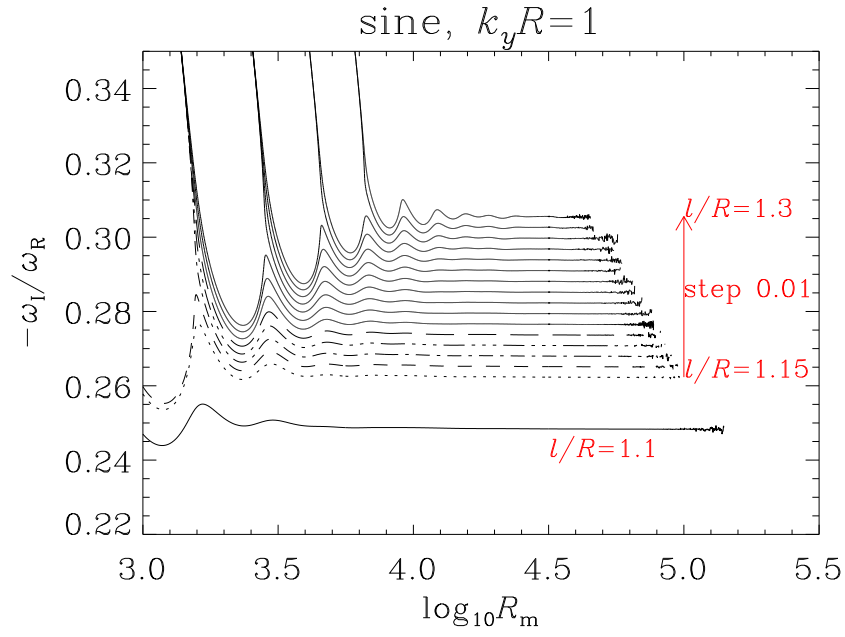


Figure 2. Dependence on the magnetic Reynolds number $[R_m]$ of the ratio of the imaginary to the real part of the eigenfrequency $[-\omega_I/\omega_R]$ of resonantly damped kink modes in coronal slabs. A “sine” profile is adopted for the equilibrium density, and the density contrast $[\rho_i/\rho_e]$ is chosen to be 10. A number of values are examined for the dimensionless transition layer width $[l/R]$, with l/R evenly spaced by 0.01 with the exception of the curve labeled $l/R = 1.1$. The axial and out-of-plane wavenumbers correspond to $k_z R = \pi/50$ and $k_y R = 1$, respectively.

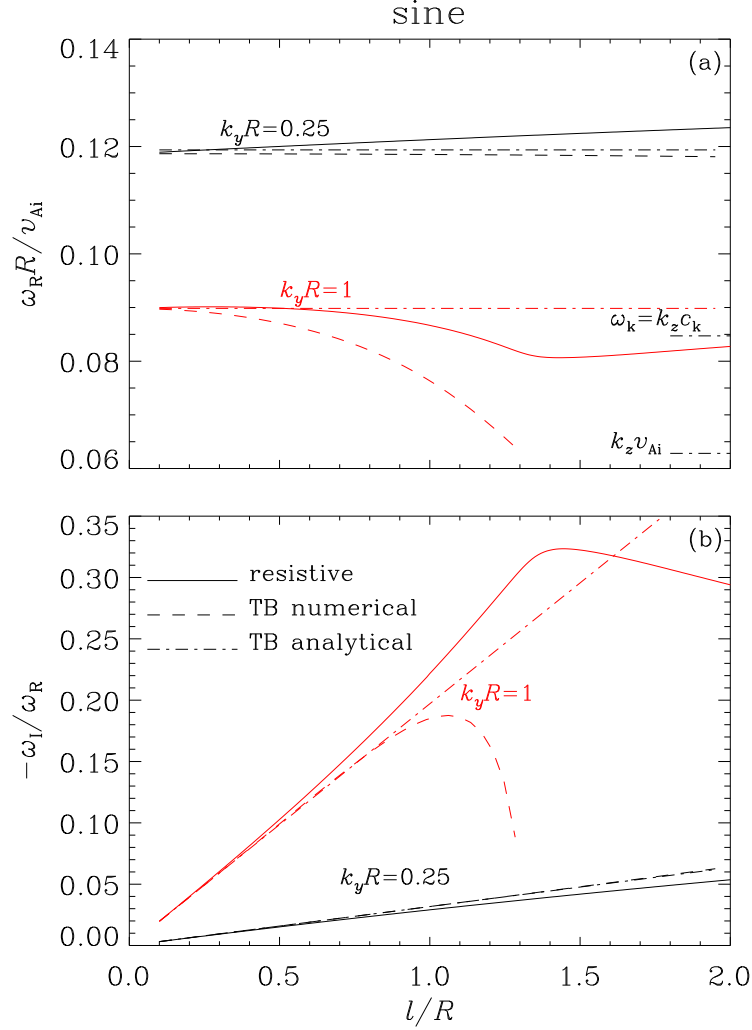


Figure 3. Dispersive properties of resonantly damped kink modes in coronal slabs. Shown here are the dependencies on the dimensionless TL width $[l/R]$ of (a) the real part of the eigenfrequency $[\omega_R]$, and (b) the ratio of the imaginary to the real part $[-\omega_I/\omega_R]$. The solid lines represent the results obtained with resistive computations, while the dashed ones correspond to the numerical solutions to the explicit DR (Equation 20) valid in the thin-boundary (TB) limit ($l/R \ll 1$). The analytical solutions to this DR, nominally valid when $k_y^2 \gg |\omega^2/\nu_A^2|$ and $k_y l \ll 1$, are plotted by the dash-dotted curves (see Equations 21 and 26 for details). Two different values of k_y are examined as labeled. For comparison, the horizontal bars represent the angular frequencies $k_z \nu_{Ai}$ and $\omega_k = k_z c_k$. A “sine” profile is adopted for the equilibrium density, the density contrast is fixed at $\rho_i/\rho_e = 10$, and the axial wavenumber is fixed at $k_z R = \pi/50$.

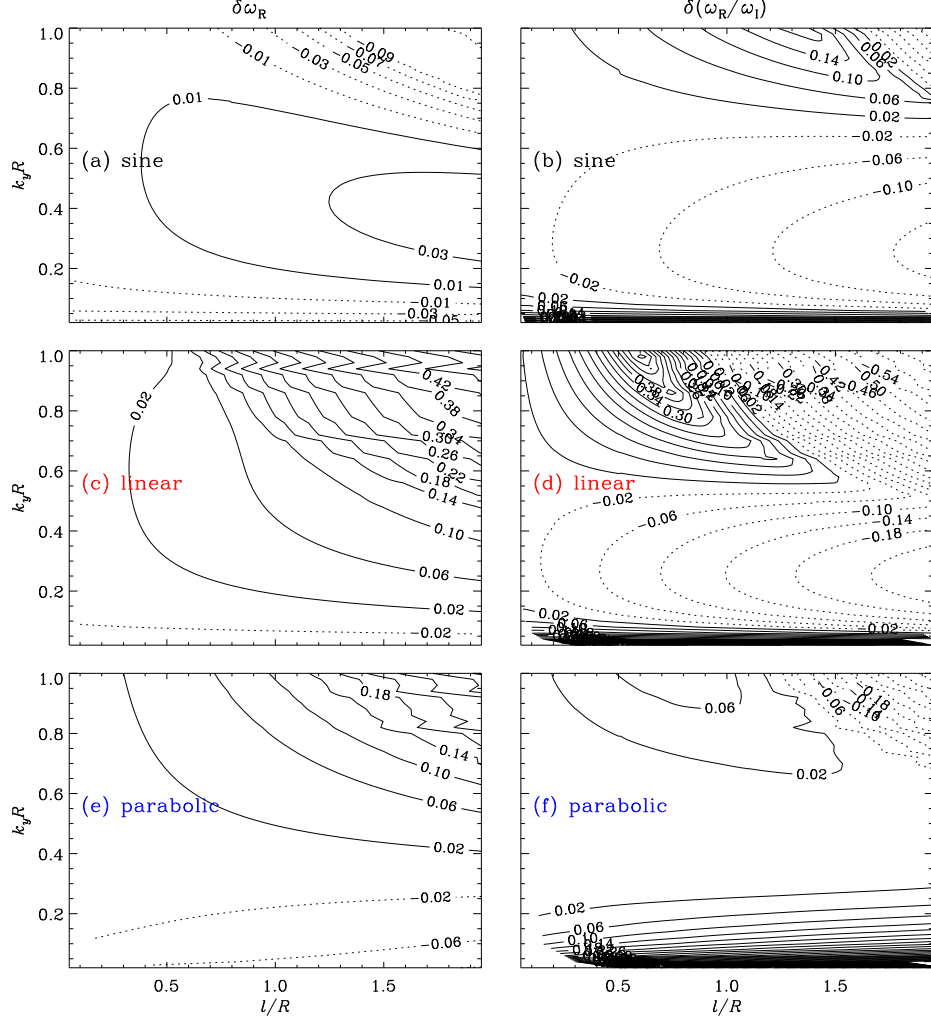
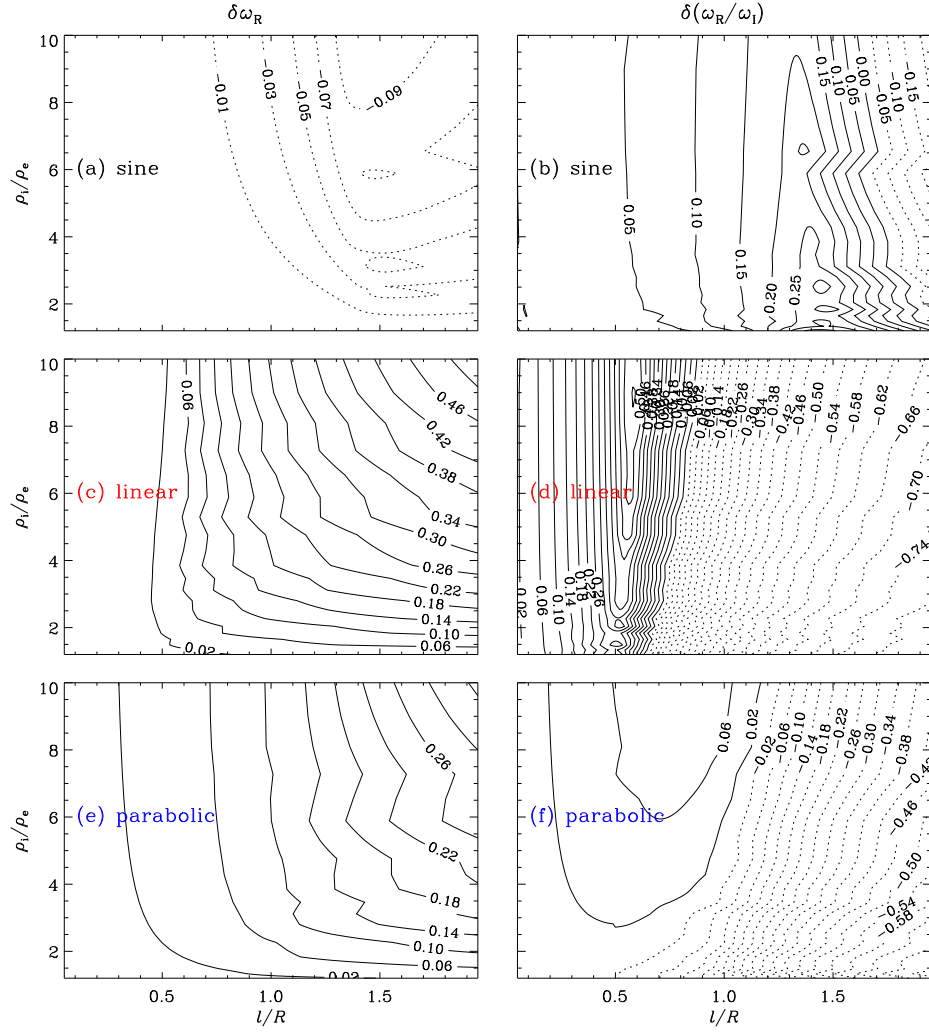


Figure 4. Comparison of the eigen-frequencies self-consistently computed in resistive MHD with the results analytically expected in the thin-boundary limit. Shown here are the distributions in the $l/R - k_y R$ plane of $\delta\omega_R$ (the left column) and $\delta(\omega_R/\omega_I)$ (right), the definitions for which are given in Equation 30. Different rows pertain to different density profiles are labeled. The contours in each panel are equally spaced, with negative (positive) values represented by the dotted (solid) curves. The pair of $[\rho_i/\rho_e, k_z R]$ is fixed at $[10, \pi/50]$.



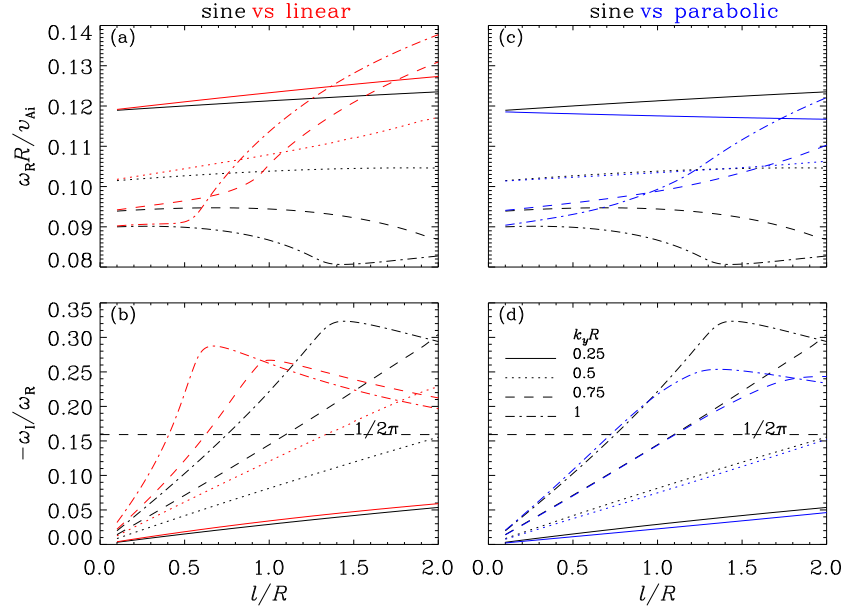


Figure 6. Influence of the density profile prescription on the dispersive properties of resonantly damped kink modes in coronal slabs. Shown here are the dependencies on the dimensionless TL width (l/R) of both the real part of the eigenfrequency (ω_R , the top row) and the ratio of the imaginary to the real part ($-\omega_I/\omega_R$, lower). Different profiles are differentiated by different colors, and a number of k_y are examined as represented by different linestyles. The horizontal dashed line in the lower row corresponds to $1/2\pi$, at which value the damping-time-to-period ratio attains unity. The pair of $[\rho_i/\rho_e, k_z R]$ is fixed at $[10, \pi/50]$.

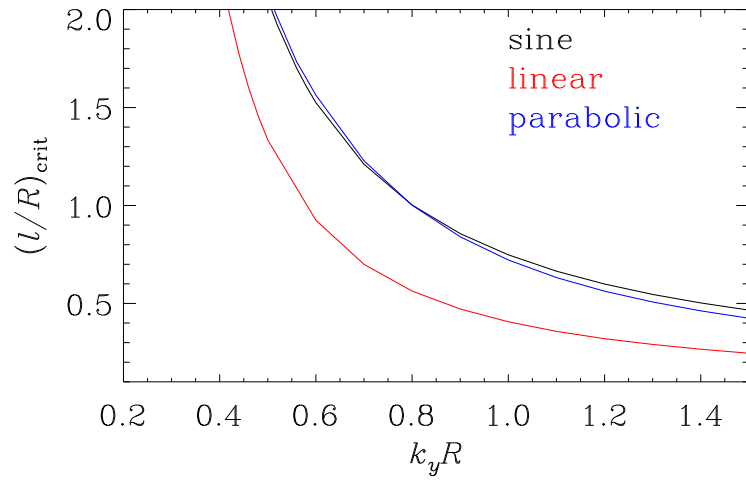


Figure 7. Influence of the density profile prescription on the dispersive properties of resonantly damped kink modes in coronal slabs. Shown here is the dependence on k_y of the critical dimensionless TL width $(l/R)_{\text{crit}}$, at which value $|\omega_I/\omega_R|$ attains $1/2\pi$. Different colors are adopted to represent different density profiles. The pair of $[\rho_i/\rho_e, k_z R]$ is fixed at $[10, \pi/50]$.

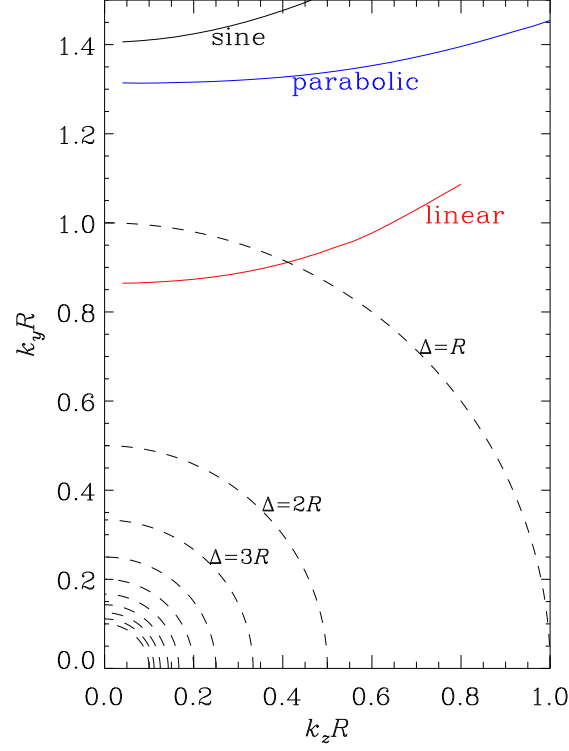


Figure 8. Influence of the density profile prescription on the dispersive properties of resonantly damped kink modes in coronal slabs. The solid curves in different colors pertain to the pair of $[k_y, k_z]$ where $|\omega_I/\omega_R|$ attains $1/2\pi$ at a fixed $l/R = 0.5$ for different density profiles as labeled. The density contrast is fixed at $\rho_i/\rho_e = 10$. Any dashed curve corresponds to those combinations of $[k_y, k_z]$ where the power spectral density drops from its maximum by a factor of e for some initial perturbation that depends on x and y as $\exp[-(x^2 + y^2)/2\Delta^2]$. A uniform spacing of R is adopted for Δ to plot the dashed curves, the outermost one pertaining to $\Delta = R$. See the text for details.